Mapping Regions with Different Bifurcation Diagrams of a Reverse-Flow Reactor

J. Khinast and D. Luss
Dept. of Chemical Engineering, University of Houston, Houston, TX 77204

A systematic method is presented for constructing maps of parameter regions with qualitatively different bifurcation diagrams of the reverse-flow reactor (RFR). These maps are most useful for the rational design and periodic operation of an RFR. The method is illustrated by two examples. The map for a single, exothermic first-order reaction contains five regions with qualitatively different bifurcation diagrams when the Damköhler number is the bifurcation variable. The high-temperature branch is isolated in two of these regions. The map for two independent, exothermic first-order reactions contains seven regions with qualitatively different bifurcation diagrams when the adiabatic temperature rise is the bifurcation parameter. Three stable periodic states exist for some values of the bifurcation variable in five of the regions. In some of these regions the intermediate state cannot be obtained upon a slow change in the concentration of the reactants. In all the examples we studied, a stability exchange of the pseudohomogeneous model occurred only at the limit points of the bifurcation diagrams. An efficient numerical scheme is presented for computing the loci of the singular points of the RFR model.

Introduction

A reverse-flow reactor (RFR) is a packed-bed reactor in which the flow direction is periodically reversed (Figure 1) to trap a hot zone within the reactor. It is one of only two types of periodic catalytic processes that have found technological applications so far (the other one is a circulating fluidized bed). The RFR concept was proposed and patented by Cottrell (1938) about 60 years ago. However, the recent applications and interest in the RFR have been motivated by its successful application to SO_2 oxidation in Russia (Boreskov et al., 1979; Boreskov and Matros, 1983). An independent patent for application of a modified RFR to the reduction of SO_2 was issued to Watson (1975). His design included inert refractory ceramics ahead of and after the catalytic section.

An RFR offers clear advantages for certain processes. The declining temperature profile in the downstream section of an RFR increases the conversion of an exothermic, equilibrium-limited reaction over that attained in an adiabatic reactor. In the destruction of dilute pollutants, an RFR avoids the need of adding fuel to a dilute mixture in order to stabilize the reaction zone, and it readily adjusts to variations in the feed load and composition. An RFR offers an opportunity of simultaneously conducting the desired reactions in the upstream section of the reactor while burning off deposited coke in the downstream (DeGroote et al., 1995). A comprehensive, recent review of the applications and studies of the RFR was presented by Matros and Bunimovich (1996).

The RFR operates under conditions for which multiple (several) periodic states exist, that is, in addition to the extinguished (low-temperature) state, there exists at least one periodic state with a hot zone in the reactor. Chumakova and Matros (1991) observed three periodic solutions for a single exothermic reaction, whereas Ivanov et al. (1992) and Salinger and Eigenberger (1996a,b) have shown that for two independent, exothermic reactions, up to five periodic solutions may exist for some parameters. Nieken et al. (1994) observed this multiplicity during the simultaneous oxidation of propylene and propane. The RFR usually leads to a symmetric period-one operation, that is, spatial variable profiles at the beginning and the end of one flow reversal are mirror images of each other, whereas the profiles are identical at the beginning and end of two flow reversals (= 1 cycle).

The rational design and operation of the RFR requires efficient prediction of its performance. Rather simple predictions may be obtained for the limiting cases of very short and

Correspondence concerning this article should be addressed to D. Luss.

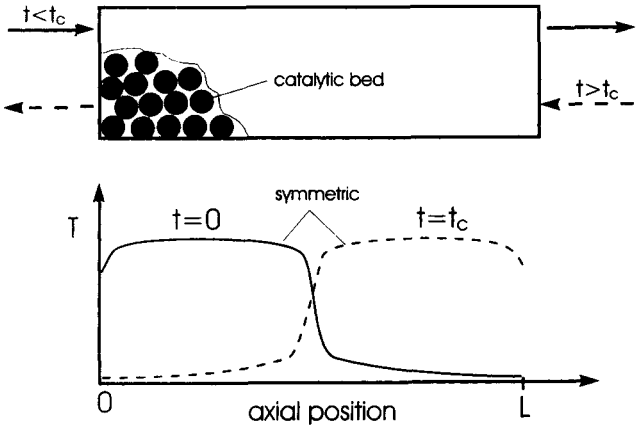

Figure 1. Schematic of the RFR for one switching cycle and of the temperature profiles at two consecutive flow switches.

infinitely long cycle periods (Matros, 1990; Eigenberger and Nieken, 1988; Nieken et al., 1995, Somani et al., 1997). Dynamic simulations of the RFR are usually rather lengthy, as the periodic states are attained only after several hundred flow reversals. The computational effort can be considerably reduced by the procedure proposed by Gupta and Bhatia (1991) of directly calculating the periodic solutions by forcing the temperature profiles at the beginning and end of a period (half cycle) to be mirror images of each other. Thus, the set of partial differential equations is solved as a spatial and temporal boundary-value problem. This procedure significantly reduces the computational effort and can determine both the stable and unstable solutions.

In practice, it is important to know the impact of changes in the operating conditions (parameters) on the various periodic states. This information is usually presented in *bifurcation diagrams*. Several investigators (Matros, 1990; Bhatia, 1991; Gupta and Bhatia, 1991; van de Beld and Westerterp, 1994; van de Beld, 1995) used numerical simulations to construct bifurcation diagrams. Chumakova and Matros (1991) used the catastrophe theory to find isolated branches in the bifurcation diagrams of conversion vs. the superficial flow velocity, using the limiting model of very short contact time to compute the periodic states. Rehacek et al. (1992) used dynamic simulations to show that asymmetric and aperiodic motions can be obtained using a two-phase model of a cooled RFR.

Recently, Salinger and Eigenberger (1996a,b) used the computational procedure proposed by Gupta and Bhatia (1991) and a numerical continuation technique to track limit points of a two-phase model. These loci were used to map parameter regions with a different number of solutions for either a single or two independent reactions. Using a Floquet stability analysis, they found that for most sets of parameters $r+1$ of the $2r+1$ periodic states were stable and symmetric. However, their calculations confirmed the finding of complex and aperiodic states by Rehacek et al. (1992) for a two-phase model, which accounted for cooling of the gas phase.

The objective of this work is to present a systematic methodology for generating global maps of parameter regions with qualitatively different bifurcation diagrams of the RFR. These maps determine, among other things, the parameters for which isolated branches of periodic states exist, and show when and how the qualitative features of the hysteresis loops change. This information is most useful for the design and periodic operation of the RFR. The method is applied to studying the behavior of an RFR in which either a single or two parallel exothermic, first-order reactions occur. Singularity theory with a distinguished parameter is applied to the periodic solutions of a distributed parameter system, and is used to determine the boundaries of the various regions.

Mathematical Model Development

Matros and Bunimovich (1996) reviewed the various models used to simulate an RFR. We apply a one-dimensional pseudohomogeneous model of an adiabatic RFR that accounts for axial heat dispersion and external mass-transfer resistance between the fluid and the catalyst. The model assumes that all the physical properties are independent of the temperature and concentration, and that the effective thermal conductivity λ_{eff} satisfies the relation (Vortmeyer and Schaefer, 1974)

$$\lambda_{\text{eff}} = (1-\epsilon)\lambda_s + \lambda_{sg}, \tag{1}$$

where

$$\lambda_{sg} = \frac{u^2(\rho c_p)_g^2}{h a_v}. \tag{2}$$

The first term in Eq. 1 accounts for the conductivity of the solid phase, the second for the effective thermal dispersion due to the heat transfer between the solid and the gas. This model has been used recently by several authors (Eigenberger and Nieken, 1988; Matros, 1989; Haynes et al., 1992, 1995; Nieken et al., 1995) to simulate an RFR. Analysis of the dynamic features of a packed-bed reactor (Pinjala et al., 1988) showed that the predictions of this model and a two-phase model are in general very similar when the temperature front moves in the downstream direction.

The dimensionless energy and species balances for two parallel first-order reactions in the RFR are

$$g_0 \equiv \frac{1}{\zeta}\frac{\partial\Theta}{\partial\tau} - \frac{1}{Pe_h}\frac{\partial^2\Theta}{\partial\xi^2} + f\frac{\partial\Theta}{\partial\xi} - \sum_{i=1}^{2} Da_i \cdot \beta_i \cdot B_i(\Theta)\cdot(1-x_i) = 0$$

$$g_i \equiv \frac{1}{Le}\frac{\partial x_i}{\partial\tau} - \frac{1}{Pe_{m,i}}\frac{\partial^2 x_i}{\partial\xi^2} + f\frac{\partial x_i}{\partial\xi} - Da_i \cdot B_i(\Theta)\cdot(1-x_i) = 0 \qquad i=1,2, \tag{3}$$

where

$$x_i = \frac{c_{i,0}-c_i}{c_{i,0}}, \qquad \Theta = \frac{T}{T_0}, \qquad \tau = \frac{t}{t_c}, \qquad \xi = \frac{z}{L} \tag{4a}$$

$$Le=\frac{ut_c}{L\epsilon},\qquad \Delta T_{ad,i}=\frac{-\Delta h_i c_{i,0}}{(\rho c_p)_g},\qquad \beta_i=\frac{\Delta T_{ad,i}}{T_0},$$

$$Pe_h=\frac{Lu(\rho c_p)_g}{\lambda_{eff}} \quad (4b)$$

$$\zeta=\frac{1}{L}\cdot\frac{t_c u(\rho c_p)_g}{(1-\epsilon)(\rho c_p)_s+\epsilon(\rho c_p)_g},\qquad Pe_{m,i}=\frac{uL}{D_{eff,i}},$$

$$\gamma_i=\frac{E_{a,i}}{RT_0} \quad (4c)$$

$$Da_i=\frac{Lk_{\infty,i}\exp[-\gamma_i]}{u},\qquad B_i(\Theta)=\frac{a_v k_{c,i}\exp\left[\gamma_i\left(\frac{\Theta-1}{\Theta}\right)\right]}{a_v k_{c,i}+k_{\infty,i}\exp\left[-\frac{\gamma_i}{\Theta}\right]}. \quad (4d)$$

The f in Eqs. 3 accounts for the flow direction and is equal to 1 (-1) for flow from the left (right). The Gupta and Bhatia (1991) procedure used by us requires integration of Eqs. 3 over one half cycle from $t=0$ to $t=t_c$, or $\tau=0$ to $\tau=1.0$.

We define

$$z^T=(\Theta-1,\ x_1,\ x_2)\qquad \boldsymbol{Pe}^T=(Pe_h,\ Pe_{m,1},\ Pe_{m,2}). \quad (5)$$

The spatial boundary conditions at $\tau=0$ are

$$\frac{\partial z}{\partial\xi}=0 \quad \text{at} \quad \xi=0;\qquad -\frac{\partial z}{\partial\xi}=\boldsymbol{Pe}\,z \quad \text{at} \quad \xi=1, \quad (6a)$$

while those for $0<\tau<1$ are

$$\frac{\partial z}{\partial\xi}=\boldsymbol{Pe}\,z \quad \text{at} \quad \xi=0;\qquad \frac{\partial z}{\partial\xi}=0 \quad \text{at} \quad \xi=1. \quad (6b)$$

The temporal symmetric boundary conditions are

$$z(\tau=0,\ \xi)=z(\tau=1,\ 1-\xi). \quad (7)$$

We write the three partial differential equations $g^T=(g_0,\ g_1,\ g_2)$ in vectorial form

$$\boldsymbol{g}(\boldsymbol{u},\ \lambda,\ \boldsymbol{p})=0, \quad (8)$$

where $\boldsymbol{u}$ is a vector of the three state variables $(\Theta,\ x_1,\ x_2)$; λ is the bifurcation (distinguished) parameter and $\boldsymbol{p}$ denotes the remaining set of parameters, which are independent of λ. The method proposed in this work uses formulas developed by Golubitsky and Schaeffer (1985) for computation of the derivatives of the branching equation directly from the original set of equations. While the computation of limit points (singular points of codimension 0) does not require the use of this procedure (Salinger and Eigenberger, 1996a), it is the most efficient one for calculating singularities of codimension ≥ 1 that are needed in the analysis presented here.

In the next section we describe the mathematical techniques used to construct the boundaries of regions with different bifurcation diagrams and to check the stability of the solutions. Readers interested just in the results and not in the details of the mathematical manipulations, may skip the next section. A highly efficient numerical method for determining the loci of the various singular points of the model is presented in the Appendix.

Prediction of Model Features

Bounding regions with qualitatively different bifurcation diagrams

We define two bifurcation diagrams to be *qualitatively similar* when the number, order, and orientation of the solutions $\boldsymbol{u}$ change in an identical way upon a continuous change in λ. We restrict the discussion here to cases in which $\boldsymbol{g}$ is a single-valued function of $\boldsymbol{u}$ and is smooth (differentiable to all orders) with respect to $\boldsymbol{u}$ and λ within the feasible region. Moreover, the branches of solutions neither intersect nor have limit points on the $\boldsymbol{u}$ and λ boundaries. All these conditions are satisfied by the model of an RFR in which several first-order reactions occur.

The boundaries of parameter regions with qualitatively similar bifurcation diagrams may be determined by application of the singularity theory with a distinguished parameter developed by Golubitsky and Schaeffer (1985). They proved that next to an organizing center (highest-order singularity) the qualitative features of the local bifurcation diagram of the universal unfolding of $\boldsymbol{g}(\boldsymbol{u},\ \lambda,\ \boldsymbol{p})=0$, which satisfies the preceding conditions, may change only if the parameter set crosses one of three hypersurfaces in the parameter space of the unfolding parameters: *hysteresis, double-limit*, and *isola* variety. The three varieties are of codimension 1, that is, variation of one parameter can generate all the qualitatively different bifurcation diagrams adjacent to these singular surfaces. Typically two limit points coalesce upon crossing the hysteresis variety, while an isolated branch of solutions appears (or disappears) upon crossing the isola variety. Crossing of either the hysteresis or isola variety typically changes by two the number of limit points of the bifurcation diagrams. Crossing a double-limit variety typically changes the relative positions of two limit points in the bifurcation diagrams. The bifurcation diagrams and their unfoldings corresponding to each of these three codimension-1 varieties are shown in Figure 2.

Uppal et al. (1976) used bifurcation analysis to map the dynamic features of the CSTR. Balakotaiah and Luss (1984, 1988) used the three varieties to divide the global parameter space of lumped reactor models into regions with qualitatively different bifurcation diagrams. For distributed reactor models $\boldsymbol{g}(\boldsymbol{u},\lambda,\boldsymbol{p})=0$ is a boundary-value problem in one to three spatial dimensions. Jensen and Ray (1982) classified the bifurcation diagrams of a cooled tubular reactor by using discretization of the differential equations. The shooting technique was applied by Nielsen and Villadsen (1983, 1985), Witmer et al. (1986), Balakotaiah et al. (1987), and Song et al. (1990) to determine the multiplicity features of distributed reactor models. Subramanian and Balakotaiah (1996) combined an implicit Liapunov-Schmidt reduction with the shooting method to classify the steady-state and dynamic features

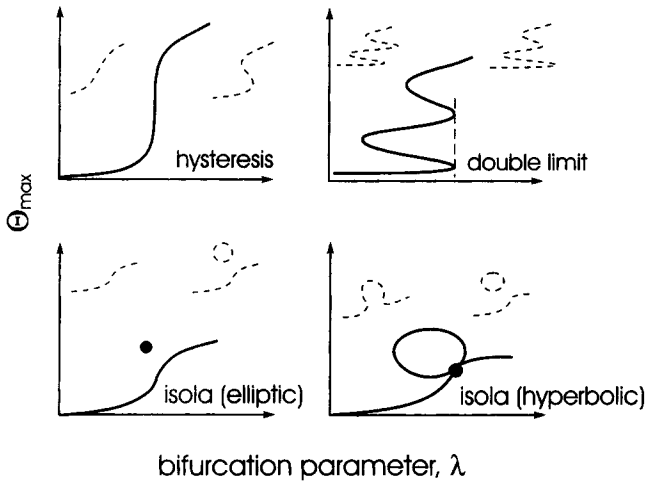

Figure 2. Bifurcation diagrams (solid lines) and their unfoldings (dashed lines) for a set of parameters on the hysteresis, double limit, and isola variety.

of various diffusion–convection–reaction problems, described by a set of differential equations in one spatial dimension. Salinger and Eigenberger (1996a,b) used bifurcation methods to compute singularities of codimension-0 (limit points) of periodic solutions of PDEs. We apply here singularity theory with a distinguished parameter to track codimension-1 singular points of the periodic RFR operation in order to map parameter regions with different bifurcation diagrams. The different boundaries of these regions, that is, the hysteresis, double-limit, and isola varieties are calculated by solving the model equations simultaneously with a set of defining conditions (Subamanian and Balakotaiah, 1996) for each singularity.

The hysteresis variety is defined by the set of conditions:

$$\boldsymbol{g}(\boldsymbol{u}, \lambda, \boldsymbol{p}) = 0 \tag{9}$$

$$\boldsymbol{L}\boldsymbol{v} = D_u\boldsymbol{g}\cdot\boldsymbol{v} = 0 \tag{10}$$

$$\boldsymbol{L}^*\boldsymbol{y} = 0 \tag{11}$$

$$\langle \boldsymbol{y}, D^2_{uu}\boldsymbol{g}\cdot(\boldsymbol{v},\boldsymbol{v})\rangle = 0, \tag{12}$$

where $D_u\boldsymbol{g}\cdot\boldsymbol{v}$ and $D^2_{uu}\boldsymbol{g}\cdot(\boldsymbol{v},\boldsymbol{v})$ are the first and second Fréchet derivatives of $\boldsymbol{g}$; $\boldsymbol{u}$ is the vector of the state variables; $\boldsymbol{v}$ and $\boldsymbol{y}$ are the eigenvector and adjoint eigenvector corresponding to the zero eigenvalue of the linearized operator $\boldsymbol{D_u g}$. Equation 12 defines the second derivative of the branching equation, which has to vanish at the hysteresis variety. Since the eigenvectors are defined except for a multiplicative constant, we choose eigenvectors of unity length,

$$\sum_{i=1}^{n} v_i^2 = 1. \tag{13}$$

The adjoint problem $\boldsymbol{L}^*\boldsymbol{y}$ may be determined by

$$\langle \boldsymbol{L}\boldsymbol{v}, \boldsymbol{y}\rangle = \langle \boldsymbol{v}, \boldsymbol{L}^*\boldsymbol{y}\rangle, \tag{14}$$

where the inner product of a real-valued n-dimensional vector function is defined by

$$\langle \boldsymbol{v}, \boldsymbol{y}\rangle = \int_0^1 \int_0^1 \sum_{i=0}^{n} (v_i y_i)\, d\tau d\xi. \tag{15}$$

The linearized operators $\boldsymbol{L}\boldsymbol{v}$ and $\boldsymbol{L}^*\boldsymbol{y}$ for the two-reaction case are given in the Appendix.

When the state vector $\boldsymbol{u}$ consists of n elements, each of Eqs. 9, 10 and 11 is a set of n equations, whereas both Eqs. 12 and 13 are single equations. The five conditions (Eqs. 9–13) generate a set of $3n+2$ equations that are solved simultaneously to determine the $3n$ variables $(\boldsymbol{u}, \boldsymbol{v}, \boldsymbol{y})$ and two parameters (λ, p_1) on the hysteresis variety. The variety is constructed by continuation with respect to one additional parameter p_2 in $\boldsymbol{p}$. The choice of the bifurcation parameter and those that are held constant depends on the application. When more than two limit points exist there may be different types of hysteresis varieties. We denote a hysteresis variety to be of type (i, j) if it is formed by the coalescence of limit points i and j. The coalescence of two hysteresis varieties forms a swallowtail.

The double-limit variety is the set of parameters for which two separated limit points occur at the same value of the bifurcation parameter, λ. Therefore, this variety is defined by the four conditions:

$$\boldsymbol{g}(\boldsymbol{u}_\alpha, \lambda, \boldsymbol{p}) = 0 \qquad \boldsymbol{g}(\boldsymbol{u}_\beta, \lambda, \boldsymbol{p}) = 0 \tag{16a}$$

$$\boldsymbol{L}\boldsymbol{v}_\alpha = 0 \qquad \boldsymbol{L}\boldsymbol{v}_\beta = 0. \tag{16b}$$

The two different limit points are denoted by the subscripts α and β. Normalization of the two eigenvectors leads to two additional relations:

$$\sum_{i=1}^{n} v_{\alpha i}^2 = 1 \qquad \sum_{i=1}^{n} v_{\beta_i}^2 = 1. \tag{17}$$

Each of the four conditions in Eq. (16) is a set of n partial differential equations. Equation 17 defines two additional conditions. These $4n+2$ equations determine $4n$ variables $(\boldsymbol{u}_\alpha, \boldsymbol{v}_\alpha, \boldsymbol{u}_\beta, \boldsymbol{v}_\beta)$ and two parameters (λ, p_1) of a double-limit point. The double-limit variety is computed by a continuation technique that determines the dependence of the two parameters on one additional parameter in $\boldsymbol{p}$. When more than two distinct limit points exist for the same λ, there are different types of double-limit varieties. We denote a double-limit variety to be of type (i, j), if it is formed when limit points i and j exist for the same value of the bifurcation variable. The limit points are ordered corresponding to their occurrence on the connected solution branch, beginning with the lowest limit point.

The isola variety is defined by the conditions:

$$\boldsymbol{g}(\boldsymbol{u}, \lambda, \boldsymbol{p}) = 0 \tag{18}$$

$$\boldsymbol{L}\boldsymbol{v} = 0 \tag{19}$$

$$\boldsymbol{L}^*\boldsymbol{y} = 0 \tag{20}$$

$$\langle \boldsymbol{y}, D_\lambda \boldsymbol{g}\rangle = 0. \tag{21}$$

While any variable may be selected to be the bifurcation variable, an isola variety exists only for some (or no) choice of this variable. Two types of isola points exist. An isolated branch appears at an *elliptic* isola point, while an isolated branch coalesces with another branch at a *hyperbolic* isola point. The conditions distinguishing between an elliptic and hyperbolic isola points require the calculation of higher derivatives of the branching equation ($g_{u\lambda}$, $g_{\lambda\lambda}$) and are not reported here. However, the varieties can be easily distinguished by inspection.

The three conditions (Eqs. 18–20) generate $3n$ equations. The normalization condition for the zero eigenvector v, Eq. 13, and the last condition (Eq. 21) are two additional equations. The $3n+2$ equations determine $3n$ variables (u, v, y) and two parameters (λ and p_1) on the isola variety. The variety is constructed by continuation with respect to a third parameter p_2. The Fréchet derivatives of g with respect to the distinguished variable λ are given in the appendix.

Stability analysis

A periodic state is stable if the amplitude of a small disturbance decreases during subsequent cycles. In contrast, the amplitude of an unstable periodic state increases from one cycle to another. Eventually, the system converges to a period-n, quasi-periodic or chaotic state. The stability of periodic states may be analyzed by Floquet theory (Iooss and Joseph, 1990), that is, by computing the eigenvalues of the *monodromy matrix* M. This method has been applied to various systems in the chemical engineering literature showing periodic states (Kevrekidis et al., 1986a,b; Gogolides et al., 1992; Croft and LeVan, 1994a,b; Salinger and Eigenberger, 1996a,b). Since our system exhibits mirror symmetry before and after one flow reversal we compute for each variable k in $u=(u_1, u_2, u_3)=(\Theta, x_1, x_2)$ a block of the monodromy matrix according to

$$m^{[k,l]}=\{m_{i,j}\}=\left\{\frac{(\hat{u}_k^{(N-i)}(\tau=1)-u_k^{(N-i)}(\tau=1))}{\delta_l^{(j)}}\right\},$$
$$i, j=1,\ldots,N, \quad (22)$$

where $\delta_l^{(j)}$ is a small perturbation of the variable l at node point j at the time $\tau=0$; and $\hat{u}_k^{(N-i)}$ and $u_k^{(N-i)}$ are the perturbed and unperturbed values of the variable k at node point $(N-i)$. The superscript $(N-i)$ in Eq. 22 reflects the symmetry of the solution. The monodromy matrix is

$$M=\begin{pmatrix} m^{[1,1]} & m^{[1,2]} & m^{[1,3]} \\ m^{[2,1]} & m^{[2,2]} & m^{[2,3]} \\ m^{[3,1]} & m^{[3,2]} & m^{[3,3]} \end{pmatrix}. \quad (23)$$

Floquet theory asserts that a periodic state is stable if all eigenvalues of M (*Floquet multipliers*) are located within a unit circle of the complex plane. The periodic orbit is unstable if the value of at least one of the Floquet multipliers exceeds this boundary.

Bifurcation Diagrams of the RFR

The periodic state of an RFR in which two parallel, exothermic, first-order reactions occur is described by Eqs. 3 and the boundary conditions (Eqs. 6 and 7). The single-reaction case is a special situation of the preceding model. In the Appendix we describe the derivation of the defining conditions for these cases and the efficient numerical procedure used to implement it. In the single-reaction case we use the Da-number as the bifurcation parameter that may be altered by changing the flow velocity. In the two-reaction case we choose the adiabatic temperature rise of component 1, β_1, which may be manipulated by changing the feed concentration as the bifurcation variable. The different types of bifurcation diagrams are then mapped in a plane that consists of at least one design parameter to enable assessment of both design and operation variables.

Single reaction with Da as a bifurcation variable

We describe here the determination of the boundaries of parameter regions with qualitatively different bifurcation diagrams of Θ_{max} vs. Da for the single-reaction case. Θ_{max} is the maximum temperature that will occur in the reactor during one cycle. Therefore, each point in the bifurcation diagram corresponds to a certain (stable or unstable) periodic orbit. In the simulations we used the following set of parameters reported by Nieken and Eigenberger (1988) for the oxidation of propane:

$$k_\infty=1.815\times10^7\ [1/s]; \qquad E_a/R=8328.6\ [K];$$
$$k_c=0.115\ [m/s]. \quad (24)$$

In all the simulations the inlet gas temperature is assumed to be

$$T_0=323\ [K]. \quad (25)$$

We ignore the influence of the velocity on the interphase mass-transfer coefficient and on the effective thermal conductivity of the bed. These effects may, if desired, easily be incorporated in the simulations. Some of the dimensionless variables defined by Eq. 4 include the residence time or the velocity, which affect the bifurcation variable, Da. These were replaced by products of dimensionless groups that do not include the residence time or the velocity, that is, they are independent of Da. Specifically, we assume that

$$\zeta\cdot Da=10^{-5}; \qquad Pe_{m,1}/Pe_h=116.0; \qquad Le\cdot Da=10^{-3}. \quad (26)$$

Figure 3 describes the hysteresis (denoted by dashed line H) and isola (solid line) varieties in the plane of β (dimensionless temperature rise) vs. the product $Pe_h\cdot Da$ (measure of reactor length). The varieties divide the plane into five regions, each with qualitatively different bifurcation diagrams. The hyperbolic isola (I_2) and the hysteresis (H) varieties intersect tangentially at a pitchfork point, P, next to which four regions with different bifurcation diagrams exist.

The bifurcation diagram in each region may be determined either by computing it for one set of parameters, or from knowledge of the pattern in one region and of the possible transitions upon crossing a specific variety. For sufficiently

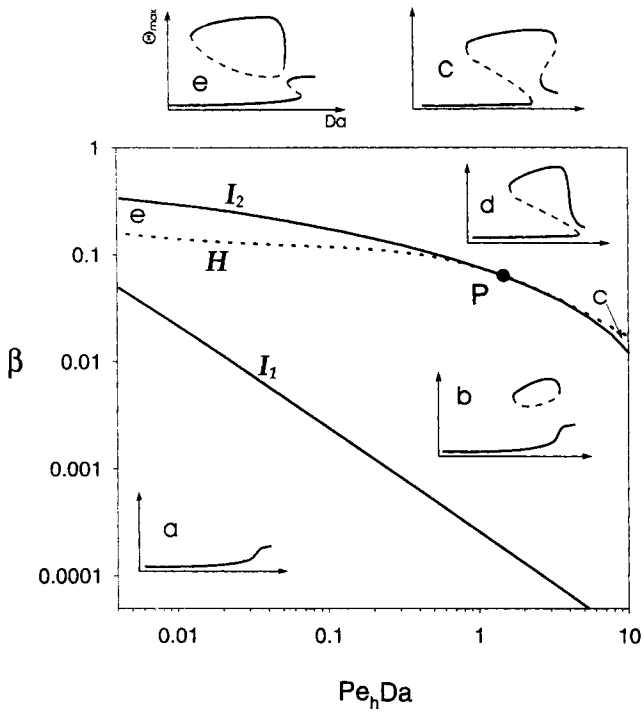

Figure 3. Five regions in the β-$Pe_h \cdot Da$ plane with qualitatively different bifurcation diagrams of Θ_{max} vs. Da (shown as insets) for an RFR in which a single, exothermic, first-order reaction occurs.

The solid lines denote an isola (I) variety; the dashed line a hysteresis (H) variety.

large values of the β and $Pe_h \cdot Da$, the bifurcation diagram of Θ_{max} vs. Da (case d in Figure 3) has two limit points. For very small Da only the extinguished state exists. A rather high temperature state exists for intermediate Da values.

Decreasing the value of β causes a transition either to region c, in which the bifurcation diagram has the shape of a mushroom, or to region e, in which the bifurcation diagram has the shape of an S plus an isola. A further decrease in β leads to region b, in which the bifurcation diagram consists of a monotonic curve and an isola. Further decrease in β leads to crossing of the elliptic isola variety (I_1) at which the isola vanishes, generating a monotonic bifurcation diagram of Θ_{max} vs. Da (denoted by a in Figure 3). In this region a high temperature zone is not trapped within the reactor, which means that the RFR operation is not beneficial.

In all simulations a stability exchange was found only at the limit points of the bifurcation diagrams, that is, at saddle-node points. We did not find any stability bifurcation similar to those found by Rehacek et al. (1992) for a two-phase model of a cooled RFR with a large difference in the thermal dispersion by the solid and gas phases. Bifurcation diagrams a, b, d, and e were previously found by Chumakova and Matros (1991) by changing one parameter (reactor-length) of a high-frequency flow-reversal model.

Two parallel reactions with β_1 as a bifurcation variable

We examine here the qualitatively different bifurcation diagrams of Θ_{max} vs. β_1 for the two-reaction case. Preliminary calculations have shown that the parameters that have the main impact on the reactor performance are the activation energies of the two reactions γ_1, γ_2, the two frequency factors $k_{\infty,1}$ and $k_{\infty,2}$, the relative adiabatic temperature rise of component 1, Y, defined as

$$Y = \frac{\beta_1}{\beta_1 + \beta_2} \tag{27}$$

and the dimensionless cycle time, ζ. The Peclet number for heat, Pe_h, has only a moderate influence on the boundaries of the various regions, and the Peclet number for mass transport, $Pe_{m,i}$, has a negligible impact. Therefore, in all the calculations we assumed that

$$Da_1 = 6.36 \cdot 10^{-5} \qquad Pe_h = 200 \qquad \text{and} \qquad Pe_{m,i} = 10^4. \tag{28}$$

Additionally, the parameters given in Eqs. 24 and 25 are left unchanged (reaction 1). The calculations were conducted for specified values of the dimensionless cycle time ζ and the ratio φ, defined as

$$\varphi = \frac{Da_2\, B_2(\Theta = 1.6)}{Da_1\, B_1(\Theta = 1.6)}. \tag{29}$$

Since the kinetic parameters of the first reaction were specified, having a constant φ ratio required adjusting the value of the frequency factor $k_{\infty,2}$ when the value of γ_2 changed.

We present maps of regions with different types of bifurcation diagrams in the plane of Y and γ_2. In all the calculations only hysteresis and double-limit varieties were found, that is, these bifurcation diagrams do not have any isolated branches. Note, that isolas may also be found in this case by choice of a different bifurcation parameter, such as Da_1 and Da_2.

Figure 4 is a typical map in the Y-γ_2 plane of regions with different bifurcation diagrams calculated for $\zeta = 0.2$ and $\varphi = 150$. Three hysteresis varieties (12, 23 and 34) and three double-limit varieties (13, 14, 24) divide the Y-γ_2 plane into seven regions with qualitatively different bifurcation diagrams. At points S ($Y = 0.9976$, $\gamma_2 = 22.296$) in Figure 4 the two hysteresis varieties 12 and 23 intersect, causing limit points 1, 2, and 3 to coalesce and form a swallowtail point. A second swallowtail point may be formed by an intersection of hysteresis varieties 23 and 34 at high γ_2 values. This intersection did not occur within the investigated range of activation energy. The boundaries shown in Figure 4 are a projection of the varieties from a three-dimensional space into a plane. Thus, point Z is not an intersection of the two hysteresis varieties 12 and 34, but is an intersection of the projections of these two varieties. The bifurcation diagram at point Z includes two hysteresis points and is rather different from that at the swallowtail point S. The bifurcation diagrams at Z and S are shown in Figure 4.

The three hysteresis varieties enclose a region in the Y-γ_2 plane within which the bifurcation diagrams of Θ_{max} vs. β_1 have four limit points. Crossing one of these three varieties leads to region b, in which the bifurcation diagrams have only

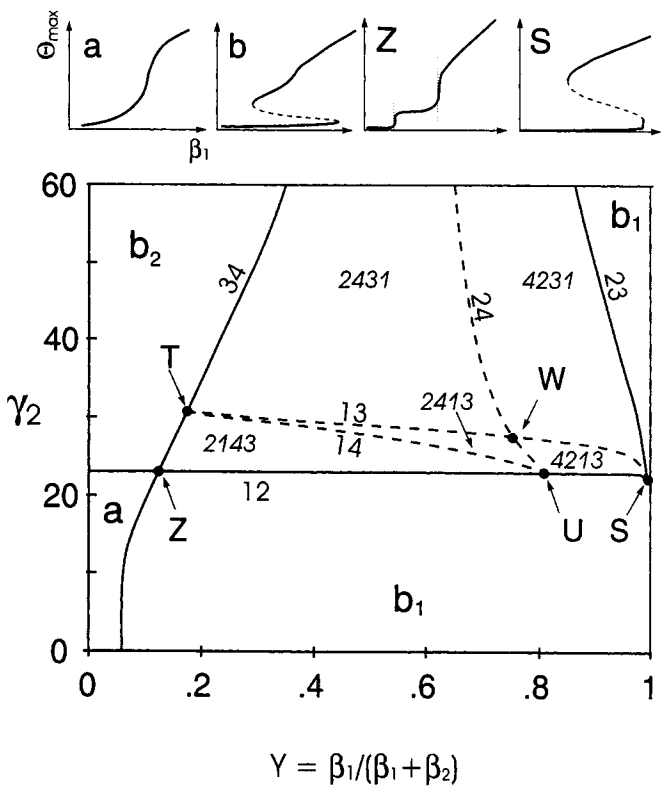

Figure 4. Regions in the γ_2–Y plane with seven qualitatively different bifurcation diagrams of Θ_{max} vs. β_1 for an RFR in which two independent, exothermic, first-order reactions occur; ζ = 0.2 and φ = 150.

The solid lines denote hysteresis varieties; the dashed lines double-limit varieties.

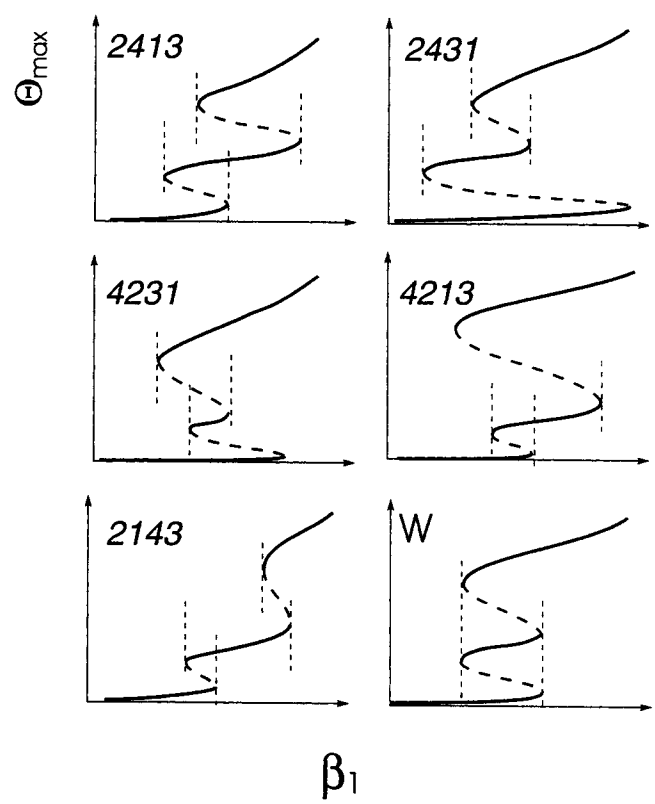

Figure 5. Bifurcation diagrams with four limit points corresponding to the regions in Figure 4; the solid (dashed) lines represent stable (unstable) periodic orbits.

two limit points, so that at most three solutions exist for any β_1 value. In region *a*, which exists for small *Y* and γ_2 values, Θ_{max} is a monotonic function of β_1. Bifurcation diagrams corresponding to regions *a* and *b* are shown on the top of Figure 4.

The (Y, γ_2) region enclosed by the three hysteresis varieties 12, 23 and 34 is divided into five subregions by the three double-limit varieties. We denote a bifurcation diagram with four limit points to be of type (i, j, k, l) if the ith limit point exists for the smallest value of the bifurcation variable, the jth limit point exists for the second smallest value, and the lth limit point for the largest value of the bifurcation variable. Figure 5 shows the five possible types of bifurcation diagrams having four limit points: 2413, 2431, 4231, 4213, and 2143.

For a bifurcation diagram, obtained in region 2413 of Figure 4, a slow increase of the bifurcation variable β_1, which may be changed by adjusting the feed concentration, causes a shift from the extinguished to the intermediate state, followed by a subsequent shift to the high-temperature state. A slow decrease of β_1 leads to a stepwise reverse shift from the high to the intermediate and then the low temperature state. A similar stepwise ignition or extinction occurs for the bifurcation diagram that exists in region 2143. For bifurcation diagram 4231 the intermediate branch cannot be reached either by a slow increase or decrease of β_1, and may be reached only by a large perturbation of either the low- or high-temperature state or by appropriate preheating of the reactor. Without proper *a-priori* knowledge of its existence, this branch of states can be easily missed in an experimental study and lead later to unexpected surprises. For bifurcation diagrams of type 2431 a slow change of β_1 enables a shift from the high-temperature branch to the intermediate one, but not from the low- to the intermediate-temperature branch. An inverse situation occurs for bifurcation diagrams of type 4213. Here, a shift from the extinguished to the intermediate state may be accomplished by a slow increase of β_1, but a shift from the ignited to the intermediate state by a slow decrease of β_1 is not possible.

The dependence of the largest Floquet multiplier on β_1 is shown in Figure 6 for a typical case in each region of the bifurcation map, Figure 4. In all the cases, the Floquet multiplier crossed unity only at the limit points of the bifurcation diagrams, that is, a stability exchange occurred only at saddle-node points. In region b_1, a sharp dip in the loci of the Floquet multiplier occurred on the branch of unstable states. In region b_2 the dip occurred on the branch of stable states. The corresponding bifurcation diagrams had an inflection point at the location of the dip.

Figure 7 describes the variation of β_1 along the hysteresis and double-limit varieties. While β_1 is rather constant along hysteresis variety 34, its value changes over several orders of magnitude along hysteresis variety 12. Similarly, the value of β_1 is rather constant along the double-limit variety 24, but

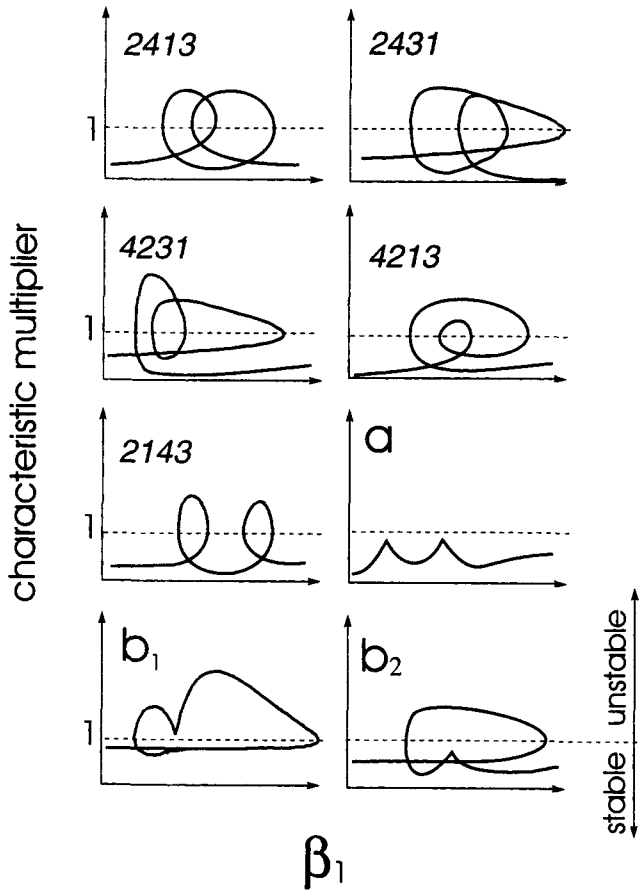

Figure 6. Characteristic multipliers of the monodromy matrix for typical cases in each of the regions in Figure 4.

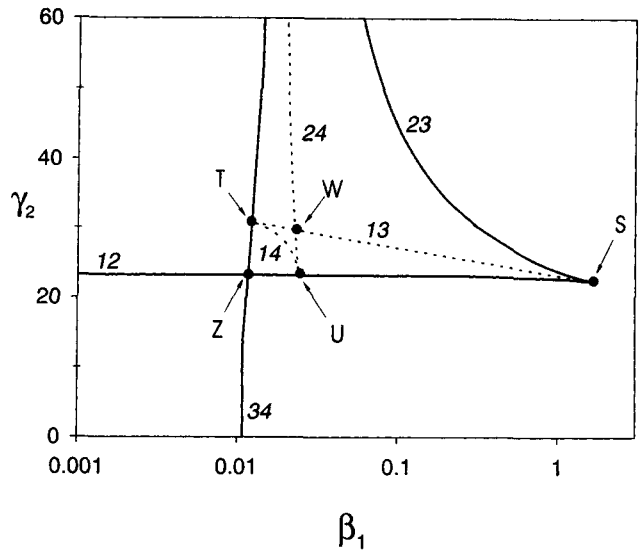

Figure 7. Values of β_1, the dimensionless adiabatic temperature rise, on the hysteresis (solid lines) and double-limit (dashed lines) varieties of the bifurcation map, Figure 4.

The numbers denote the type of double limit and hysteresis variety.

variety 24, but changes by two orders of magnitude along the double-limit variety 13.

The maximum bed temperature and the maximum conversion of component 1 along the hysteresis and double-limit varieties are presented in Figure 8. The maximum temperature along the double-limit variety 24 exceeds those that can be attained on any hysteresis variety. It is of interest to note that the change in the maximum temperature or conversion is much smoother than that of the varieties in Figure 4. For example, the two hysteresis varieties 12 and 23 form a cusp at the swallowtail point S in Figure 4. The two merge smoothly at S in Figure 8. Similarly, the double-limit varieties 14 and 13 form a cusp at point T in the bifurcation map, but merge smoothly at T in Figure 8. The maximum temperature along the hysteresis variety (34), which passes through point T, is rather independent of variation in the γ_2 value.

Figure 9 is a bifurcation map computed for the same parameters as Figure 4, except for $\varphi = 20$ instead of $\varphi = 150$. The smaller value of φ decreases the size of the (Y, γ_2) region for which five perodic states exist. Further decrease of φ eventually leads to the disappearance of this region.

Discussion and Conclusions

The method presented here enables a systematic mapping of regions of parameters with qualitatively different bifurcation diagrams of the RFR. Knowledge of these regions and the corresponding diagrams provides the reactor designer with valuable guidance about the potential impact of a change in an operating condition (runaway), the robustness of the design, and indicates potential start-up and control problems. For example, the existence of isolated branches of solutions, such as those in regions b or e of Figure 3 (the single-reaction case) indicates that a special start-up policy will be needed to attain this high-temperature branch. Similarly, the existence of a nested branch of periodic states such as those in region 4231 of Figure 4 (the two-reaction case) requires a special start-up procedure to reach the intermediate temperature branch. In many two-reaction systems the intermediate branch is the one with the highest yield of the desired product. Knowledge of the shape of the bifurcation diagram enables one to design proper start-up and control policies.

The examples presented here illustrate the rich and intricate nature of bifurcation diagrams of the adiabatic RFR. While an adiabatic CSTR has two types of bifurcation diagrams of temperature vs. Da, a monotonic dependence and one with an S shape, the adiabatic RFR has five different types. These five diagrams are similar to those obtained in a cooled CSTR in which a first-order reaction with a high activation energy occurs and the coolant is kept at the feed temperature (Balakotaiah and Luss, 1983). Numerical difficulties prevented us from computing the varieties shown in Figure 3 for $Pe_h \cdot Da$ values less than 4×10^{-3}. However, the similarity of the map to those obtained for a cooled CSTR and approximate numerical calculations strongly suggest that the two isola branches form a cusp at lower values of $Pe_h \cdot Da$, while the hysteresis variety extends to $Pe_h \cdot Da = 0$. Thus, a direct transition between bifurcation diagram type d (S-type multiplicity) and a unique solution for all Damköhler numbers occurs for all $Pe_h \cdot Da$ smaller than that at the cusp formed by the two isola branches.

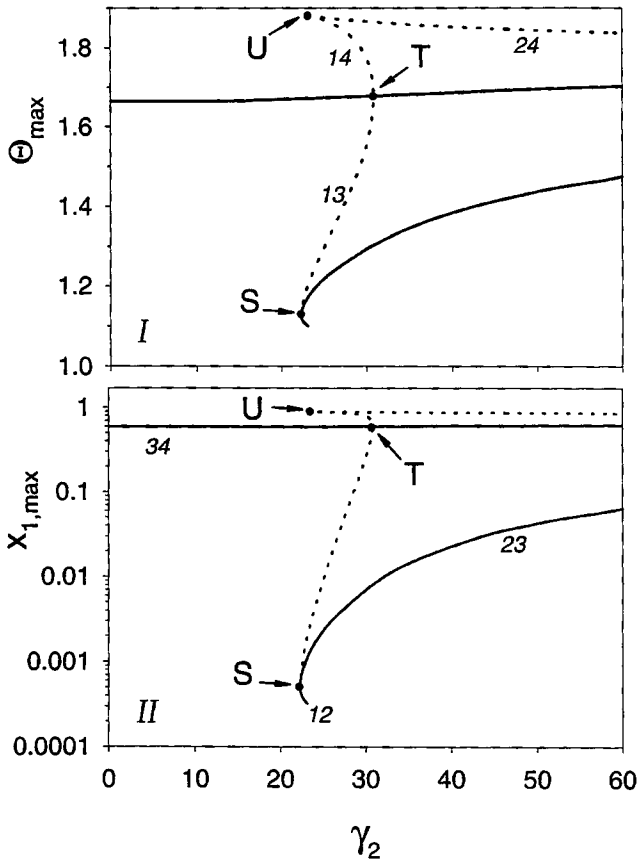

Figure 8. Maximum bed temperature (I) and reactant 1 conversion (II) on the hysteresis (solid lines) and double-limit (dashed lines) varieties of the bifurcation map, Figure 4.

We show only the temperature and conversion at the higher limit point of the double-limit variety. The numbers in I (II) denote the type of double-limit (hysteresis) variety.

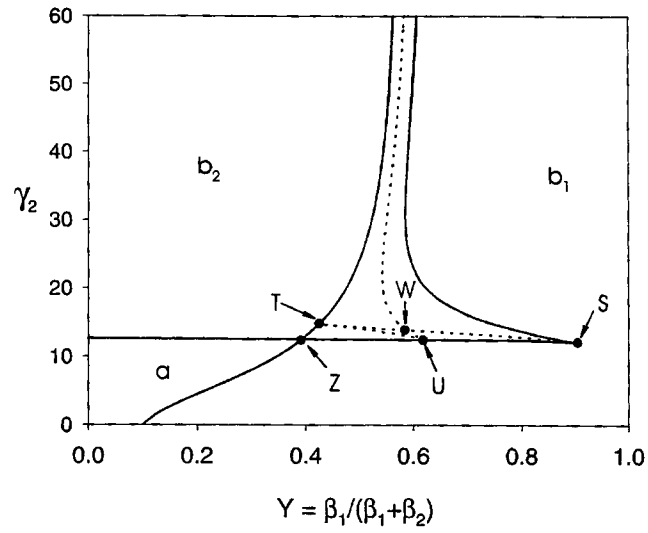

Figure 9. Bifurcation map for the two reaction case; except for $\varphi = 20$, all the parameters are the same as in Figure 4.

The finding of stability exchange only at limit points of the bifurcation diagrams does not imply that other types of dynamic stability exchange cannot occur in the RFR. Our numerical findings are restricted to the set of parameters used in our simulations. Salinger and Eigenberger (1996b) reported similar observations to ours. Rehacek et al. (1992) reported the finding of period-n and aperiodic states for a two-phase model of the RFR in which the gas phase is cooled. The complex dynamics may be due to that cooling and/or the large difference in the thermal conductivity of the gas and solid phase.

The maps of the codimension-1 varieties are constructed in a plane of two parameters. The existence of isolated branches of solutions for the single-reaction case and their lack for the two-reaction case is due to the use of different bifurcation variables. Using Da as the bifurcation variable would lead to isolated solutions in both the single- and two-reaction case. Similarly, using β_1 as the bifurcation variable will generate only connected branches of solutions in both cases. Qualitatively different maps of bifurcation diagrams may be found when one either selects different values for the remaining parameters in p, or constructs a map for another pair of parameters. The reason is that the universal unfolding of the highest-order singular point of the RFR model usually contains more than two parameters, so that all the regions of different bifurcation diagrams cannot be found in a single planar map. To determine all the feasible types of bifurcation diagrams, one needs to find, by a numerical continuation procedure, the highest-order singular point and then construct its universal unfolding. This is a rather laborious numerical task and will not be discussed here. For most practical applications in which many of the parameters are fixed for a specific set of reactions and catalyst, bifurcation maps of the type presented here provide all the needed design information.

The numerical procedure of combining a shooting method, continuation techniques and Newton's method with standard Broyden-update was found to be very efficient for determining the loci of various singularities of the model.

The procedure used in this study to determine the different types of bifurcation diagrams of the RFR can also be applied to other periodic processes involving distributed parameter systems.

Acknowledgments

We gratefully acknowledge the financial support of the Austrian Science Foundation (Grant No. J01173-TEC), the ACS-PRF, and the computing time grants by the Pittsburgh Supercomputing Center and by the Center for Advanced Molecular Computations at the University of Houston. We are most thankful to Prof. V. Balakotaiah for many helpful discussions.

Notation

a_v = specific surface area, m^2/m^3
$B_i(\Theta)$ = temperature dependence of reaction rate
c_i = concentration of species i, mol/m^3
c_p = heat capacity, $J/(kg \cdot K)$
$d\bar{Y}$ = correction vector of Newton step
$D_{eff,i}$ = effective diffusion coefficient of species i, m^2/s
Da_i = Damköhler number of species i
$E_{a,i}$ = activation energy of species i, J/mol
f = vector of nonlinear residual equations

h = heat-transfer coefficient, W/(K·m^2)
$-\Delta h_i$ = heat of the reaction i, J/mol
$k_{c,i}$ = mass-transfer coefficient for species i, m/s
L = reactor length, m
Le = Lewis number, defined by Eq. 4
$\boldsymbol{m}$ = block of the monodromy matrix
N = number of node points in space direction
n = number of variables and equations
$\boldsymbol{Pe}$ = vector of Peclet numbers defined by Eq. 5
R = universal gas constant, J/(mol·K)
ρc_p = heat capacity, J/(m^3·K)
r = number of reactions
t = time, s
t_c = time of one flow switch (half cycle time), s
T = temperature, K
ΔT_{ad} = adiabatic temperature rise, K
u = superficial gas velocity, m/s
x_i = conversion of species i
z = axial coordinate, m
$\boldsymbol{z}$ = vector defined by Eq. 5
β_i = dimensionless adibatic temperature rise, defined by Eq. 4
ϵ = bed voidage
ρ = density, kg/m^3
λ_s = solid conductivity, W/(m·K)
λ_{sg} = effective conductivity accounting for heat transfer between solid and gas defined by Eq. 2, W/(m·K)
Θ = dimensionless temperature, defined by Eq. 4
ξ = dimensionless reactor length

Subscripts and superscripts

0 = feed
ad = adiabatic
g = gas phase
k = number of actual Newton step
s = solid phase

Literature Cited

Balakotaiah, V., and D. Luss, "Multiplicity Features of Reacting Systems; Dependence of the Steady-states of a CSTR on the Residence Time," *Chem. Eng. Sci.*, **38**, 1709 (1983).

Balakotaiah, V., and D. Luss, "Global Analysis of the Multiplicity Features of Multi-Reaction Lumped-Parameter Models," *Chem. Eng. Sci.*, **39**, 865 (1984).

Balakotaiah, V., G. Witmer, R. Hu, and D. Luss, "Dependence of the Multiplicity Features of an Isothermal Catalytic Reaction on External and Internal Transport Resistances," *Chem. Eng. Commun.*, **58**, 195 (1987).

Balakotaiah, V., and D. Luss, "Global Mapping of Parameter Regions with a Specific Number of Solutions," *Chem. Eng. Sci.*, **43**, 957 (1988).

Bhatia, S. K., "Analysis of Catalytic Reactor Operation with Periodic Flow Reversal," *Chem. Eng. Sci.*, **46**, 361 (1991).

Boreskov, G. K., Yu. Sh. Matros, and O. V. Kiselev, "Catalytic Processes Carried Out Under Nonstationary Conditions: Thermal Front in a Fixed Bed of Catalyst," *Kinet. Catal.*, **20**(3), 773 (1979).

Boreskov, G. K., and Yu. Sh. Matros, "Unsteady-state Performance of Heterogeneous Catalytic Reactions," *Catal. Rev.-Sci. Eng.*, **25**(4), 551 (1983).

Chumakova, N. A., and Yu. Sh. Matros, "Isolating Laminar-flow Regimes with Periodic Sweep Reversal in a Fixed Catalyst Layer," *Teor. Osn. Khimi. Tekhnol.*, **25**, 369 (1991).

Cottrell, F. G., "Purifying Gases and Apparatus Therefor," U.S. Patent No. 2,171,733 (June 21, 1938).

Croft, D. T., and M. D. LeVan, "Periodic States of Adsorption Cycles—I. Direct Determination and Stability," *Chem. Eng. Sci.*, **49**, 1821 (1994a).

Croft, D. T., and M. D. LeVan, "Periodic States of Adsorption Cycles—II. Solution Spaces and Multiplicity," *Chem. Eng. Sci.*, **49**, 1831 (1994b).

DeGroote, A. M., G. F. Froment and Th. Koblynski, "Synthesis Gas Production from Natural Gas in a Fixed Bed Reactor with Reversed Flow," *Proc. USPC-2 Meeting*, St. Louis (1995).

Deuflhard, P., E. Hairer, and J. Zugck, "One-step and Extrapolation Methods for Differential-Algebraic Systems," *Numer. Math.*, **51**, 1 (1987).

Eigenberger, G., and U. Nieken, "Catalytic Combustion with Periodic Flow Reversal," *Chem. Eng. Sci.*, **43**, 2109 (1988).

Finlayson, B. A., "Nonlinear Analysis in Chemical Engineering," McGraw Hill, New York (1980).

Gogolides, E., H. H. Sawin, and R. A. Brown, "Direct Calculation of Time-Periodic States of Continuum Models of Radio-Frequency Plasmas," *Chem. Eng. Sci.*, **47**, 3839 (1992).

Golubitsky, M., and D. G. Schaeffer, *Singularities and Groups in Bifurcation Theory*, Vol. 1, Springer-Verlag, New York (1992).

Gupta, V. K., and S. K. Bhatia, "Solution of Cyclic Profiles in Catalytic Reactor Operation with Periodic Flow Reversal," *Comput. Chem. Eng.*, **15**, 229 (1991).

Haynes, T. N., C. Georgakis, and H. S. Caram, "The Application of Reverse Flow Reactors to Endothermic Reactions," *Chem. Eng. Sci.*, **47**, 2927 (1992).

Haynes, T. N., C. Georgakis, and H. S. Caram, "The Design of Reverse Flow Reactors for Catalytic Combustion Systems," *Chem. Eng. Sci.*, **50**(3), 401 (1995).

Hood, P., "Frontal Solution Program for Unsymmetric Matrices," *Int. J. Numer. Methods Eng.*, **10**, 379 (1976).

Iooss, G., and D. D. Joseph, *Elementary Stability and Bifurcation Theory*, 2nd ed., Springer-Verlag, New York (1990).

Ivanov, Yu. V., A. S. Noskov, Yu. Sh. Matros, and G. A. Bunimovich, "Multiplicity of States in Catalytic Reactors with Periodic Reversal of Gas Mixture Flow," *Teor. Osn. Khimi. Tekhnol.*, **26**, 228 (1992).

Jensen, K. F., and W. H. Ray, "The Bifurcation Behavior of Tubular Reactors," *Chem. Eng. Sci.*, **37**, 199 (1982).

Kevrekidis, I. G., R. Aris, and L. D. Schmidt, "Some Common Features of Periodically Forced Reacting Systems," *Chem. Eng. Sci.*, **41**, 1263 (1986a).

Kevrekidis, I. G., R. Aris, and L. D. Schmidt, "The Stirred Tank Forced," *Chem. Eng. Sci.*, **41**, 1549 (1986b).

Matros, Yu. Sh., *Catalytic Processes under Unsteady State Conditions*, Elsevier, Amsterdam (1989).

Matros, Yu. Sh., "Performance of Catalytic Processes under Unsteady Conditions," *Chem. Eng. Sci.*, **45**, 2097 (1990).

Matros, Yu. Sh., and G. A. Bunimovich, "Reverse-flow Operation in Fixed Bed Catalytic Reactors," *Catal. Rev. Sci. Eng.*, **38**, 1 (1996).

Nieken, U., G. Kolios, and G. Eigenberger, "Fixed-bed Reactors with Periodic Flow Reversal: Experimental Results for Catalytic Combustion," *Cat. Today*, **20**, 355 (1994).

Nieken, U., G. Kolios, and G. Eigenberger, "Limiting Cases and Approximate Solutions for Fixed-bed Reactors with Periodic Flow Reversal," *AIChE J.*, **41**, 1915 (1995).

Nielsen, P. H., and J. Villadsen, "Absorption with Exothermic Reaction in a Falling Film Column," *Chem. Eng. Sci.*, **38**, 1439 (1983).

Nielsen, P. H., and J. Villadsen, "An Analysis of Multiplicity Pattern on Models for Simultaneous Diffusion Chemical Reaction and Absorption," *Chem. Eng. Sci.*, **40**, 571 (1985).

Pinjala, V., Y. C. Chen and D. Luss, "Wrong-way Behavior of Packed-bed Reactors: II. Impact of Thermal Dispersion," *AIChE J.*, **34**, 1663 (1988).

Press, W. H., S. A. Teukolsky, W. T. Vetterling, and B. P. Flannery, *Numerical Recipes in Fortran*, Cambridge Univ. Press, Cambridge (1992).

Rehacek, J., M. Kubicek, and M. Marek, "Modeling of a Tubular Reactor with Flow Reversal," *Chem. Eng. Sci.*, **47**(9–11), 2897 (1992).

Salinger, A. G., and G. Eigenberger, "The Direct Calculation of Periodic States of the Reverse-flow Reactor: 1. Methodology and Propane Combustion Results," *Chem. Eng. Sci.*, **51**, 4903 (1996a).

Salinger, A. G., and G. Eigenberger, "The Direct Calculation of Periodic States of the Reverse Flow Reactor: 2. Multiplicity and Instability," *Chem. Eng. Sci.*, **51**, 4915 (1996b).

Seydel, R., and V. Hlavacek, "Role of Continuation in Engineering Analysis," *Chem. Eng. Sci.*, **42**, 1281 (1987).

Somani, M., S. Viswanath, J. Khinast, and D. Luss, "Maximum Temperature in a Reverse-flow Reactor with Two Independent Reactions," *Chem. Eng. Sci.*, **52**, 2483 (1997).

Song, X., L. D. Schmidt, and R. Aris, "Shooting Method for Bifurcation Analysis of Boundary Value Problems," *Chem. Eng. Sci.*, **44**, 967 (1989).

Subramanian, S., and V. Balakotaiah, "Classification of Steady-State and Dynamic Behavior of Distributed Reactor Models," *Chem. Eng. Sci.*, **51**, 401 (1996).
Uppal, A., W. H. Ray, and A. B. Poore, "The Classification of the Dynamic Behavior of Continuous Stirred Tank Reactors—Influence of Reactor Residence Time," *Chem. Eng. Sci.*, **31**, 205 (1976).
van de Beld, B., and K. R. Westerterp, "Air Purification by Catalytic Oxidation in a Reactor with Periodic Flow Reversal," *Chem. Eng. Technol.*, **17**, 217 (1994).
van de Beld, B., PhD Thesis, Univ. of Twente, Enschede, The Netherlands (1995).
Vortmeyer, D., and R. J. Schaefer, "Equivalence of One- and Two-phase Models for Heat Transfer Processes in Packed Beds: One Dimensional Theory," *Chem. Eng. Sci.*, **29**, 484 (1974).
Watson, E. W., "Method and Apparatus for Reacting for Sulfur Dioxide and Natural Gas," U.S. Patent No. 3,865,927 (1975).
Witmer, G., V. Balakotaiah, and D. Luss, "Finding Singular Points of Two Point Boundary Value Problems," *J. Comput. Phys.*, **65**, 244 (1986).

Appendix

Derivation of defining conditions

We describe here the defining conditions for the two-reaction case described by the set of three Eqs. 3 and the boundary conditions (Eqs. 6 and 7). The single-reaction case is a special, simplified case of the two reactions.

The linearized operator $\boldsymbol{Lv}$ is

$$\boldsymbol{Lv}=\begin{pmatrix} \frac{1}{\zeta}\frac{\partial v_1}{\partial \tau}-\frac{1}{Pe_h}\frac{\partial^2 v_1}{\partial \xi^2}+\frac{\partial v_1}{\partial \xi}-\sum_{i=1}^{2} Da_i\beta_i\left[\frac{\partial B_i}{\partial \Theta}v_1(1-u_{i+1})-B_i v_{i+1}\right] \\ \frac{1}{Le}\frac{\partial v_2}{\partial \tau}-\frac{1}{Pe_{m,1}}\frac{\partial^2 v_2}{\partial \xi^2}+\frac{\partial v_2}{\partial \xi}-Da_1\left[\frac{\partial B_1}{\partial \Theta}v_1(1-u_2)-B_1 v_2\right] \\ \frac{1}{Le}\frac{\partial v_3}{\partial \tau}-\frac{1}{Pe_{m,2}}\frac{\partial^2 v_3}{\partial \xi^2}+\frac{\partial v_3}{\partial \xi}-Da_2\left[\frac{\partial B_2}{\partial \Theta}v_1(1-u_3)-B_2 v_3\right] \end{pmatrix}. \quad \text{(A1)}$$

The corresponding spatial boundary conditions at $\tau=0$ are

$$\frac{\partial \boldsymbol{v}}{\partial \xi}=0 \quad \text{at} \quad \xi=0; \qquad -\frac{\partial \boldsymbol{v}}{\partial \xi}=\boldsymbol{Pe}\,\boldsymbol{v} \quad \text{at} \quad \xi=1, \quad \text{(A2a)}$$

while those for $0<\tau\le 1$ are

$$\frac{\partial \boldsymbol{v}}{\partial \xi}=\boldsymbol{Pe}\,\boldsymbol{v} \quad \text{at} \quad \xi=0; \qquad \frac{\partial \boldsymbol{v}}{\partial \xi}=0 \quad \text{at} \quad \xi=1. \quad \text{(A2b)}$$

The corresponding temporal boundary conditions are

$$\boldsymbol{v}(\tau=0,\,\xi)=\boldsymbol{v}(\tau=1,\,1-\xi). \quad \text{(A3)}$$

Using Eqs. 14 and 15 the adjoint problem $\boldsymbol{L}*\boldsymbol{y}$ is

$$\boldsymbol{L}^*\boldsymbol{y}=\begin{pmatrix} -\frac{1}{\zeta}\frac{\partial y_1}{\partial \tau}-\frac{1}{Pe_h}\frac{\partial^2 y_1}{\partial \xi^2}-\frac{\partial y_1}{\partial \xi}-\sum_{i=1}^{2} Da_i\frac{\partial B_i}{\partial \Theta}(1-u_{i+1})\left[\beta_i y_1+\frac{Le\,y_{i+1}}{\zeta}\right] \\ -\frac{\partial y_2}{\partial \tau}-Le\left\{\frac{1}{Pe_{m,1}}\frac{\partial^2 y_2}{\partial \xi^2}+\frac{\partial y_2}{\partial \xi}\right\}+Da_1B_1[\,\beta_1 y_1\zeta+Le\cdot y_2] \\ -\frac{\partial y_3}{\partial \tau}-Le\left\{\frac{1}{Pe_{m,2}}\frac{\partial^2 y_3}{\partial \xi^2}+\frac{\partial y_3}{\partial \xi}\right\}+Da_2B_2[\,\beta_2 y_1\zeta+Le\cdot y_3] \end{pmatrix}. \quad \text{(A4)}$$

The corresponding spatial boundary conditions at $\tau=0$ are

$$\frac{\partial \boldsymbol{y}}{\partial \xi}=-\boldsymbol{Pe}\,\boldsymbol{y} \quad \text{at} \quad \xi=0; \qquad -\frac{\partial \boldsymbol{y}}{\partial \xi}=2\boldsymbol{Pe}\,\boldsymbol{y} \quad \text{at} \quad \xi=1, \quad \text{(A5a)}$$

while those for $0<\tau\le 1$ are

$$\frac{\partial \boldsymbol{y}}{\partial \xi}=0 \quad \text{at} \quad \xi=0; \qquad -\frac{\partial \boldsymbol{y}}{\partial \xi}=\boldsymbol{Pe}\,\boldsymbol{y} \quad \text{at} \quad \xi=1. \quad \text{(A5b)}$$

The corresponding temporal boundary conditions are

$$\int_0^1 (\boldsymbol{v}^T\boldsymbol{y}\,|_{\tau=1}-\boldsymbol{v}^T\boldsymbol{y}\,|_{\tau=0})\,d\xi=0. \quad \text{(A6)}$$

The second Fréchet derivative $D^2_{uu}\boldsymbol{g}\cdot(\boldsymbol{v},\boldsymbol{v})$ is computed from the equations:

$$D^2_{uu}g\cdot(v,v)=g''=\begin{pmatrix}-\sum_{i=1}^{2} Da_i\beta_i\left[\frac{\partial^2 B_i}{\partial\Theta^2}v_1^2(1-u_{i+1})-2\frac{\partial B_i}{\partial\Theta}v_1v_{i+1}\right]\\ -Da_1\left[\frac{\partial^2 B_1}{\partial\Theta^2}v_1^2(1-x_1)-2\frac{\partial B_1}{\partial\Theta}v_1v_2\right]\\ -Da_2\left[\frac{\partial^2 B_2}{\partial\Theta^2}v_1^2(1-x_2)-2\frac{\partial B_2}{\partial\Theta}v_1v_3\right]\end{pmatrix}. \quad (A7)$$

Condition 12 of the hysteresis singularity becomes

$$\langle y, D^2_{uu}g\cdot(v,v)\rangle=\int_0^1\int_0^1 y^T g''\,d\tau\,d\xi=0. \quad (A8)$$

For the determination of isola loci, the derivative of the branching equation with respect to the bifurcation parameter is required. The Fréchet derivative $D_\lambda g$ with $\lambda=Da_1$, ($Da_2=0$), is

$$D_\lambda g=g_\lambda=\begin{pmatrix}\frac{1}{Da_1\zeta}\frac{\partial\Theta}{\partial\tau}-\frac{1}{Da_1 Pe_h}\frac{\partial^2\Theta}{\partial\xi^2}-\beta_1\cdot B_1(\Theta)\cdot(1-x_1)\\ \frac{1}{Da_1 Le}\frac{\partial x_1}{\partial\tau}-\frac{1}{Da_1 Pe_{m,1}}\frac{\partial^2 x_1}{\partial\xi^2}-B_1(\Theta)\cdot(1-x_1)\end{pmatrix}. \quad (A9)$$

Clearly, any parameter can be chosen as the bifurcation parameter, but it is not certain that an isolated branch exists.

Condition 21 becomes:

$$\langle y, D_\lambda g\rangle=\int_0^1\int_0^1 y^T g_\lambda\,d\tau\,d\xi=0. \quad (A10)$$

Since the zero eigenvector v of L is defined up to a multiplicative constant, the normalization condition 13 is introduced. The value of the bifurcation parameter at a limit point is defined by the zero eigenvector and the normalization condition. The condition of the hysteresis variety (Eq. 12) requires the zero eigenvector of the adjoint system L^*. At a limit point (and a hysteresis locus), both the linearized and the adjoint problem, Lv and L^*y, are singular and have a zero eigenvector for the same set of parameters. Requiring $L^*y=0$ and normalizing y leads to a redundant equation, because the zero eigenvalue is already determined by $Lv=0$. Since normalization of y is necessary in order not to converge to the trivial solution $y=0$, the nth equation of $L^*y=0$ has to be omitted in computing the zero eigenvector of the adjoint problem, in order not to overdetermine the linear system. However, the omitted equation has to be satisfied, and may be used as a check on the singular points.

Numerical procedure

The loci of the different singularities were determined by a shooting method in combination with a continuation technique. This method required the smallest computational execution time and storage capacity.

In the shooting method, a boundary-value problem (BVP) is integrated for a guessed initial value at boundary A until the boundary conditions at the other end of the domain B are satisfied. Thus, the BVP is transformed into a set of nonlinear algebraic equations, that is, the boundary conditions at B, which may be solved by Newton's method. When the solution is continued with respect to a parameter, it does not change significantly between two continuation steps. Therefore, the Jacobian matrix needed for one Newton step can be updated by Broyden's method, which significantly decreases the computation time. In contrast to the relaxation method, a relatively small number of unknowns has to be solved and a small Jacobian matrix is inverted. Another advantage of the shooting method is that a standard solver for initial-value problems with a predefined accuracy can be used.

Either space or the time dimension can be chosen as the direction of shooting. The derivatives in the second direction have to be discretized using traditional techniques. We used shooting in the time direction, which enables easy computation of the monodromy matrix. The method of orthogonal collocation on finite elements was used to discretize the spatial coordinate using 50–80 node points on a symmetric grid (Finlayson, 1980). The spatial first-order derivatives in the mass balances were approximated by a backward difference scheme to minimize oscillations due to large mass–Peclet numbers without significant change in the profiles. The integrals defining the various varieties were computed by Gaussian quadrature. The extrapolation code LIMEX for implicit differential-algebraic systems (Deuflhard et al., 1987) with a relative tolerance of $5\cdot10^{-7}$ was used to integrate the ordinary differential equations.

After discretization of the spatial derivatives, the resulting system has the form

$$g_d(w,\lambda,p)=0 \quad (A11a)$$

$$g_a(w,\lambda,p)=0, \quad (A11b)$$

where g_d denotes the set of ordinary differential equations, g_a the additional algebraic equations that define the singularities, and w the vector of the discrete state variables,

$$w(\tau) = (w_1^{(1)}, w_2^{(1)}, w_3^{(1)}, \ldots, w_M^{(1)}, w_1^{(2)}, \ldots, w_i^{(j)}, \ldots, w_1^{(N)}, w_2^{(N)}, w_3^{(N)}, \ldots, w_M^{(N)}), \quad \text{(A12)}$$

where the superscript, j denotes the jth node point, and the subscript i denotes the ith variable. This ordering results in a banded Jacobian matrix with the smallest bandwidth. The IVP

$$\frac{dw}{d\tau} = F(w, \lambda, p), \quad \text{(A13)}$$

where F is a vector of nonlinear functions, is solved for the guessed initial vector $w(0)$. The numerical effort associated with the time integration was minimized by analytically providing the banded Jacobian matrix of F in Eq. A13. The solution vector at the end of the period, $w(1)$, is a function of $w(0)$, that is,

$$w(1) = f(w(0), \lambda, p) = w(1, w(0), \lambda, p). \quad \text{(A14)}$$

The required mirror symmetry of the spatial profiles before and after a flow reversal give the time BCs

$$w_i^j(0) - w_i^{N-j+1}(1, w(0), \lambda, p) = 0 \qquad i = 1, \ldots, M \quad j = 1, \ldots, N. \quad \text{(A15)}$$

Equation A11b and Eq. A15 form a set of nonlinear algebraic equations,

$$\tilde{g}(w(0), \lambda, p) = 0, \quad \text{(A16)}$$

which is solved simultaneously for the variables $w(0)$, λ, and one parameter p_1 of p.

A continuation technique was used to compute the loci of the singularities as a function of a parameter (Seydel and Hlavacek, 1987). If w is the solution vector at $\tau = 0$ and p_2 the continuation parameter in p, Eq. A16 is augmented by the single equation

$$s^2 - |w - w_0|^2 - (\lambda - \lambda_0)^2 - (p_1 - p_{1,0})^2 - (p_2 - p_{2,0})^2 = 0, \quad \text{(A17)}$$

where s is the step size and the subscript 0 denotes the values at the previous step. The resulting nonlinear set of equations

$$f(Y) = 0 \quad \text{(A18)}$$

was solved numerically by a Newton-Raphson method, where the correction of the kth iterate is

$$dY_{[k]} = J_{[k-1]}^{-1} \cdot f(Y_{[k-1]}) \qquad \text{with} \quad dY_{[k]} = Y_{[k]} - Y_{[k-1]}, \quad \text{(A19)}$$

where Y denotes the solution vector of the state variables at each node point, and J is the Jacobian of Eq. A18, which cannot be determined analytically.

The maximum number of state variables and node points in our calculations was $M = 12$ and $N = 80$, that is, not more than $N \cdot M = 960$ equations. Thus, inverting of the Jacobian matrix is by far less expensive than the numerical approximation of J, since the IVP has to be integrated in the time direction $N \cdot M$ times. It is therefore advantageous to use methods that update the Jacobian at every Newton step without explicitly recomputing it. We used Broyden's update

$$J_{[k]} = J_{[k-1]} + \frac{[(f_k - f_{k-1}) - J_{[k-1]} \cdot dY_k] \cdot dY_k^T}{dY_k^T \, dY_k}, \quad \text{(A20)}$$

which requires only one function evaluation (Eq. A18) per iteration step (Press et al., 1992). This procedure is even more useful, when the update strategy is used in the continuation procedure, as it is sufficient to compute a numerical approximation of the Jacobian matrix only for the first Newton step of the first continuation step. For the following steps the approximated Jacobian of the preceding continuation step is used. The convergence of one Broyden step, which can be interpreted as a secant method, is lower than quadratic. Thus, Broyden's method requires approximately two to three times more steps than Newton's method. The main advantage of Broyden's method is that each step requires only one function evaluation, while Newton's method requires $N \cdot M$. If the function evaluations are the time-consuming step in the computation, Broyden's method reduces the computation time significantly.

The continuation step size, s, can be adjusted similarly to the step-size control of an initial-value solver. Beginning with an initial choice for s, a multiplicative factor determines the step size for the next step, depending on the number of iteration steps in the actual continuation step. In this work the step-size control was adjusted such that six Broyden steps were needed for convergence to the new solution. This enabled use of relatively large step sizes with a small number of iteration steps.

In order to provide a good initial guess for the next continuation step, the solution is extrapolated. A linear extrapolation gave the best convergence:

$$Y_{\text{guess}} = Y_0 + \frac{s}{s_0}(Y_0 - Y_{00}) \quad \text{(A21)}$$

Here the index 0 denotes the solution at the actual successful step and 00 the solution of the preceding step. This procedure enabled tracking of the solution even around sharp cusp points.

We also tested the relaxation method used by Salinger and Eigenberger (1996a,b) for the RFR. Here both the spatial and temporal gradients were discretized with a finite-element approach, and the resulting set of about 2×10^4 algebraic equations was solved by Newton's method. In this case, the computation of the Jacobian matrix is inexpensive compared to inversion of the Jacobian matrix, which has about 4×10^8 entries. In order to invert this matrix, a frontal solver (Hood,

1976) was used, since the integral conditions destroy the banded structure of the Jacobian. The method was stable and showed excellent convergence. However, limitations on storage capacity and execution time did not allow grid sizes of more than 30 node points in time and 60 node points in space direction, which may be too restrictive if steep temperature profiles occur in the reactor.

For our specific problem the implementation described earlier was approximately five times faster than the relaxation method and required limited memory due to the small size of the global Jacobian matrix. Thus, the model problem could be solved easily on a small desktop computer. Additionally, in the shooting method time integration can be performed with any desired accuracy. If a higher spatial or temporal resolution is required by the problem or if more variables occur in the system, our method becomes increasingly faster compared to the relaxation method. Above a certain number of node points and variables, the relaxation method requires excessive computer time, since storage limitations become critical even if a frontal method is used to prevent uncontrolled writing of the core memory to the hard disk. Convergence of both the numerical methods is similar.

The computation of the monodromy matrix can be implemented easily by perturbing each variable. When we remove the columns and rows of the Jacobian matrix concerning the parameters and the integral conditions, we can use the relation

$$J = I - M \tag{A22}$$

to get a new "high-quality" estimate of the Jacobian matrix. Consequently, the computation of the monodromy matrix is done at moderate additional effort.

In general, low-dimensional singularities provided an adequate initial guess for computing higher dimensional singularities. First, a bifurcation diagram was computed by continuing Eq. 9 with respect to the distinguished parameter λ. The solution vector $\boldsymbol{u}$ at the approximate limit points was stored. A limit point needs to satisfy Eqs. 9 and 10. The approximation of $\boldsymbol{u}$ and an arbitrary guess of the eigenvector $\boldsymbol{v}$ led to convergence to the exact limit points. Next, the loci of the limit points were tracked as a function of another parameter (p_1) until one reached a cusp point. Again, the values of $\boldsymbol{u}$ and $\boldsymbol{v}$ at the approximate hysteresis point and a guess of the adjoint eigenvector $\boldsymbol{y}$ were used to determine the exact hysteresis point, which satisfies the four Eqs. 9–12. Elliptic and hyperbolic isola points are found at an extremum point of the the continued limit loci.

Manuscript received Nov. 10, 1996, and revision received Apr. 10, 1997.